THE JOURNAL OF BIOLOGICAL CHEMISTRY VOL. 285, NO. 31, pp. 24078–24088, July 30, 2010

Peroxisomal Plant 3-Ketoacyl-CoA Thiolase Structure and Activity Are Regulated by a Sensitive Redox Switch*[S]

Received for publication, January 20, 2010, and in revised form, April 12, 2010 Published, JBC Papers in Press, May 12, 2010, DOI 10.1074/jbc.M110.106013

Valerie E. Pye[‡1], Caspar E. Christensen[‡], James H. Dyer[§], Susan Arent[‡2], and Anette Henriksen[‡3]

From the [‡]Protein Chemistry Group, Carlsberg Laboratory, Gamle Carlsberg Vej 10, DK-2500 Valby, Denmark and the [§]Department of Chemistry and Biochemistry, Montclair State University, Upper Montclair, New Jersey 07043

The breakdown of fatty acids, performed by the β-oxidation cycle, is crucial for plant germination and sustainability. β-Oxidation involves four enzymatic reactions. The final step, in which a two-carbon unit is cleaved from the fatty acid, is performed by a 3-ketoacyl-CoA thiolase (KAT). The shortened fatty acid may then pass through the cycle again (until reaching acetoacetyl-CoA) or be directed to a different cellular function. Crystal structures of KAT from *Arabidopsis thaliana* and *Helianthus annuus* have been solved to 1.5 and 1.8 Å resolution, respectively. Their dimeric structures are very similar and exhibit a typical thiolase-like fold; dimer formation and active site conformation appear in an open, active, reduced state. Using an interdisciplinary approach, we confirmed the potential of plant KATs to be regulated by the redox environment in the peroxisome within a physiological range. In addition, co-immunoprecipitation studies suggest an interaction between KAT and the multifunctional protein that is responsible for the preceding two steps in β-oxidation, which would allow a route for substrate channeling. We suggest a model for this complex based on the bacterial system.

Fatty acids are fundamental biomolecules that are abundant in all life forms. With their enormous variation in chain length and degree of saturation, they are essential for energy storage, form structural entities in biomembranes, and serve as signaling molecules. Fatty acids are broken down in a cyclic manner, two carbons at a time, to generate a range of products by the process known as β-oxidation (1). In higher plants (2) and yeast (3) β-oxidation of all forms of fatty acid occurs in the peroxisomes. In plants, β-oxidation is essential for a plethora of physiological roles including responses to senescence and starvation, fatty acid turnover, and the regulation of plant lipid composition. Germinating seeds depend on β-oxidation for the mobilization and release of energy stored in the seed (4). *Arabidopsis thaliana* seeds deficient in β-oxidation enzymes are unable to germinate without an external sugar source; they have large and unusual peroxisomes and accumulate C16–C20 fatty acids (5, 6). β-Oxidation is also responsible for the synthesis of jasmonic acid (7) and indole-3-acetic acid (auxin) via conversion from indole-3-butyric acid (8), which serve as crucial plant hormones regulating plant development and responses to biotic and abiotic stress. Hydrogen peroxide, produced as a byproduct during β-oxidation, is used by catalase to oxidize different toxins (*e.g.* alcohols) and plays an important role in cellular signaling (9).

β-Oxidation comprises four reactions. First, the CoA-activated acyl chain is oxidized to 2-*trans*-enoyl-CoA by an acyl-CoA oxidase (10), producing H_2O_2 as a byproduct. The double bond is then reduced by 2-*trans*-enoyl hydratase forming L-3-hydroxyacyl-CoA followed by oxidation by NAD^+-dependent L-3-hydroxyacyl-CoA dehydrogenase. Both the hydratase and dehydrogenase activities are performed by a multifunctional protein (MFP)[4] (11, 12). 3-Ketoacyl-CoA thiolase (KAT) performs the last step of β-oxidation, thiolytically cleaving a two-carbon unit from 3-ketoacyl-CoA (13). The shortened fatty acyl-CoA can then be subjected to further rounds of β-oxidation or directed to other pathways. In mammals there are two distinct pathways for β-oxidation; very long chain fatty acids and bile acid intermediates are shortened in peroxisomes, whereas medium to long chain mono- and dicarboxylic fatty acids, methyl-branched fatty acids, and prostaglandins are broken down in mitochondria (14). In both mitochondrial and prokaryotic β-oxidation systems trifunctional multi-enzyme complexes (comprising MFP and KAT activities) exist allowing for metabolite channeling (15–18). The crystal structure of the *Pseudomonas fragi* trifunctional enzyme complex is known and consists of two α-subunits (hosting MFP functions; hereafter referred to as *Pf*MFP) and two β-subunits (hosting KAT functions; hereafter referred to as *Pf*KAT) in a dynamic complex (16). Plants contain a number of isozymes for each step in β-oxidation; the acyl-CoA oxidases are best defined with regard to having

* This work was supported by the Danish Natural Science Research Council, which provided a postdoctoral stipend through DANSYNC (to S. A.) and synchrotron beam time.

[S] The on-line version of this article (available at http://www.jbc.org) contains supplemental "Discussion," Figs. S1 and S2, Table S1, and a movie.

The atomic coordinates and structure factors (codes 2WU9 and 2WUA) have been deposited in the Protein Data Bank, Research Collaboratory for Structural Bioinformatics, Rutgers University, New Brunswick, NJ (http://www.rcsb.org/).

[1] To whom correspondence may be addressed: School of Biochemistry and Immunology, Trinity College Dublin, Dublin 2, Ireland. Fax: 353-18964257; E-mail: vpye@tcd.ie.

[2] Present address: Danisco Ltd., Edwin Rahrs Vej 38, 8220 Brabrand, Denmark.

[3] To whom correspondence may be addressed. Fax: 45-33274708; E-mail: anette@crc.dk.

[4] The abbreviations used are: MFP, multifunctional protein; ACAT, acetoacetyl-CoA thiolase; KAT, 3-ketoacyl-CoA thiolase; PDB, Protein Data Bank; DTT, dithiothreitol; CSH, cysteamine; CSSC, cystamine; TLS, translation/libration/screw; bis-Tris, 2-[bis(2-hydroxyethyl)amino]-2-(hydroxymethyl)-propane-1,3-diol; L-, loop-; r.m.s.d., root mean square deviation; *Pf*, *Pseudomonas fragi*; *At*, *Arabidopsis thaliana*; *Ha*, *Helianthus annuus*; *Sc*, *Saccharomyces cerevisiae*; *Hs*, *Homo sapiens*; *Bn*, *Brassica napus*; YT medium, 16 g of Bacto Tryptone, 10 g of Bacto Yeast Extract, 5g of NaCl per liter of distilled H_2O, pH adjusted with 5 M NaOH.

different but overlapping substrate specificities. Communication between the isoforms via a protein-protein complex, similar to that found in *P. fragi*, could direct and controls the flow of metabolites through β-oxidation, but to date no such complex in plants has been reported.

There are two distinct forms of 3-ketoacyl-CoA thiolases. Type I is 3-ketoacyl-CoA thiolase (EC 2.3.1.16), a catabolic enzyme performing the reverse Claisen condensation reaction involved in, for example, the β-oxidation cycle. Type II thiolase is acetoacetyl-CoA thiolase (ACAT; EC 2.3.1.9) and is involved in the anabolic mevalonate pathway performing Claisen condensation. *Arabidopsis* has been shown to possess three KAT genes that encode three peroxisomal KAT isoforms (1, 2, and 5.2) and one cytosolic isoform lacking the N-terminal 43 residues (5.1) and two ACAT genes that encode four cytosolic ACAT isoforms (1.1, 1.2, 2.1, and 2.2) and one peroxisomal isoform (1.3) (13). In *Arabidopsis,* KAT2 is the major type I thiolase isoform present during germination; it seems to be important for triacylglycerol synthesis during seed development as well (6). KAT1 and KAT5 are not abundant in seedlings, and their roles are less well defined; KAT5 is possibly involved in flavonoid biosynthesis (13). KAT2 is reported to be active for the full range of fatty acid lengths from acetoacetyl-CoA upward (6). Thus, in contrast to the first step involving substrate-specific acyl-CoA oxidases, the last step of β-oxidation is seemingly unspecific. The first structure of KAT was solved from *Saccharomyces cerevisiae* (*Sc*KAT) (19, 20). This structure has a typical thiolase-like fold, is a homodimer, and presumably is in an active state. The structure of KAT2 from *Arabidopsis* (*At*KAT2) was solved later and also shows a homodimer with a thiolase-like fold (21). However, the *At*KAT2 structure is noticeably different from the *Sc*KAT structure; a disulfide bridge is formed involving the presumed active site nucleophile, causing the active site to be inaccessible to substrate and resulting in a change in the loop structure that caps the active site and a different dimer arrangement. A regulation of β-oxidation by redox potential was suggested; however, they did not produce either a structure of *At*KAT2 in an active, reduced state or any results that suggested oxidation taking place within a biologically relevant redox range. Recently, a human peroxisomal KAT (*Hs*KAT) structure was deposited in the PDB database by the Structural Genomics Consortium (PDB code 2IIK). *Hs*KAT is also in the active, reduced state.

Peroxisomes provide a challenging environment for enzyme stability. The redox environment of the peroxisome traditionally was considered stable and reducing due to the presence of catalase and its role in the breakdown of H_2O_2 derived from photorespiration, oxidative processes, and the decomposition of radical oxygen species (22, 23). However, H_2O_2 is now recognized as an important signaling molecule in both plants and animals (for a review see Ref. 9), and plant peroxisomes have been shown to be net producers of H_2O_2, releasing it to the cytosol (24, 25) (for a review see Ref. 26). The subcellular distribution of H_2O_2 is unknown, but the total concentration of H_2O_2 in unstressed leaves has been measured as high as 3.6 μmol/g (fresh weight) translating to an average of 3.6 mM (27, 28). The finding that the diene containing fluorescent probe BODIPY-PTS1 is oxidized in the peroxisomes of rat fibroblasts upon incubation with eicosanoic and phytanic acids suggests that the redox state of this organelle is unstable despite the redox buffering effects of the antioxidant defense systems present in peroxisomes (29). Stressing the need for regulation even further, catalase itself is inhibited at prolonged exposure to H_2O_2 generated at 2 nmol/(ml min) particularly in the absence of NADPH (30–34). Additionally, peroxisomes have been shown to change their morphology dramatically in response to H_2O_2 stresses (35). The inactivation of catalase by H_2O_2 would lead to a breakdown of the peroxisomal antioxidant defense system giving rise to toxic conditions, oxidative damage, and eventually cell death. Therefore a stable and balanced intracellular redox environment is crucial for all cells; a control point in the β-oxidation cycle would aid the control of the redox conditions in the peroxisome.

Here we present results demonstrating that the redox state and activity of *At*KAT2 are affected under biologically relevant conditions as well as the crystal structures of two plant thiolases, *At*KAT2 and sunflower *Ha*KAT (*Helianthus annuus* (*Ha*KAT)), in a reduced, open, active conformation to high resolution. We discuss the potential redox control of β-oxidation and as initiated from our co-immunoprecipitation pulldown assays, we suggest a possible complex formation with MFP. For completeness we have included in the supplemental material a comparison of the KAT structures presented here with other available peroxisomal type I KAT structures at a structural and substrate binding level.

EXPERIMENTAL PROCEDURES

Cloning, Expression, and Protein Purification—The full-length *Ha*KAT construct (36) was recloned to remove the N-terminal signaling sequence and insert a C-terminal His_6 tag. The construct for *Ha*KAT (17–449) was made using forward (5′-GGAATTCCATATGCCCTCTTCTACTTCTTCATCCTTGG-3′) and reverse (5′-GAATTGCGGCGTAGTGATGGTGATGGTGATGTTTAGCTTAATTGCAC-3′) primers. The resulting PCR fragment was ligated into a pSTblue-1 vector using the Perfectly Blunt ligation kit (Novagen). The purified plasmid was cut with restriction enzymes NdeI and NotI (New England Biolabs), and these sites were used to insert the PCR product into the pET24b expression vector (Novagen) followed by transformation of super competent XL1-Blue cells (Stratagene). Protein expression was carried out using BL21(DE3) cells. An expression construct encoding *At*KAT2-(36–462) with an N-terminal enterokinase excisable His_6 tag was prepared in pET46 Ek/LIC from clone pda03502 (Riken) using ligation independent cloning technology (Novagen) and the primers 5′-GACGACGACAAGATGGCTGGGGACAGTGCTGCATAT-3′ and 5′-GAGGAGAAGCCCGGTCAGGCGTCCTTGGACAA-3′. Successful cloning was verified by colony PCR and sequencing, and the construct was used to transform RosettaGami2(DE3) cells by electroporation. Both proteins were expressed and purified in the same manner. 1 liter of 2×YT medium supplemented with the appropriate antibiotics was inoculated with a 1/50 overnight culture and grown to A_{600} = 0.5 at 37 °C. Cells were then cooled to

25 °C before induction with 1 mM isopropyl 1-thio-β-D-galactopyranoside and incubation (shaking) at 25 °C for 18 h. Cell pellets were resuspended in a prechilled solution of 50 mM Tris-HCl, 200 mM NaCl, pH 7.7, and lysed with Bug-Buster (Sigma; 1/10 dilution) and Benzonase nuclease (Novagen; 1/1000 dilution) for 1 h at room temperature. The lysed cell pellets were centrifuged at 18,000 × *g* for 1 h, and the supernatant was applied to a 5-ml Ni^{2+} affinity column (Amersham Biosciences). After washing, the protein was eluted by an imidazole gradient. Protein fractions were assessed by SDS-PAGE, concentrated using a Vivaspin20 30,000 molecular weight cut-off filter device (Sartorius), and applied to a HiLoad 26/60 Superdex 200 prep grade (Amersham Biosciences) size exclusion column pre-equilibrated and run with 50 mM Tris-HCl and 200 mM NaCl, pH 7.7, at 4 °C. Protein fractions were again assessed by SDS-PAGE and then dialyzed overnight against 20 mM Tris-HCl, 150 mM NaCl, 2 mM EDTA, 5% (v/v) glycerol, and 2 mM DTT, pH 9.0.

Thiolase Activity Assay—The activity of *At*KAT2 was determined spectroscopically by monitoring the absorbance increase at 232 nm due to the formation of new acyl-CoA ester bonds (37). All buffers were deoxygenated by purging in an anaerobic glove box for 1 h. The reactions, consisting of 50 μM acetoacetyl-CoA and 100 μM CoA in 35 mM Tris-HCl and 100 mM NaCl, pH 8.5, were started by the addition of 5 nM *At*KAT2 preincubated with 20 mM cysteamine (CSH; Sigma) or 10 mM cystamine (CSSC; Sigma) at 25 °C. The enzyme preparations were diluted 2500× before sampling, resulting in final concentrations of CSH and CSSC of 8 and 4 μM, respectively. The absorbance change at 232 nm was recorded in a quartz microcuvette with a lambda-45 UV-visible spectrophotometer equipped with a Peltier thermal control element set to 25 °C (PerkinElmer Life Sciences). Background reactions containing the buffer and CSH or CSSC were recorded and used to normalize the data. The half-lives were determined by fitting the equation for exponential decay to the data. Acetoacetyl-CoA and CoA were prepared immediately before mixing, and concentrations were checked by UV spectroscopy using ϵ_{257} = 16,840/M cm for CoA and ϵ_{260} = 16,000/M cm for acetoacetyl-CoA with $\epsilon_{260}/\epsilon_{232}$ = 1.89 (38).

Determination of Reduction Potential of AtKAT2—Tryptophan fluorescence of 5 μM *At*KAT2 in 35 mM Tris-HCl and 100 mM NaCl, pH 8.5, was recorded after a 15-min incubation at 25 °C with varying ratios of CSH to CSSC keeping the total concentration of sulfur constant. 50-μl reactions were prepared in half-area UV 96-well microplates (Corning 3679, Corning Inc.), and wavelength scans were recorded in a fluorescence plate reader (SpectraMAX EM/Gemini, Molecular Devices) exciting with 285 nm UV-light and reading emission from 325 to 450 nm with a 325-nm cut-off filter and photomultiplier sensitivity set to medium. Control experiments with 4 mM H_2O_2 or 1 mM DTT were included. The emission reading at 333 nm was plotted against $[CSH]^2/[CSSC]$, and the midpoint of transition was found to be 0.17 M by fitting a two-state function with variable slopes to the data (Equation 1).

$$f(x) = \frac{(\alpha_0 + \beta_0 \cdot x) + \left((\alpha_1 + \beta_1 \cdot x) \cdot \exp\left(\frac{m(x - c_{50\%})}{R \cdot T}\right)\right)}{1 + \exp\left(\frac{m(x - c_{50\%})}{R \cdot T}\right)} \quad \text{(Eq. 1)}$$

Here α_n and β_n represent the *y* axis intercept and slope of the first ($n = 0$) and second ($n = 1$) linear parts of the curve, *R* is the gas constant, *T* is the temperature and $c_{50\%}$ and *m* represent the midpoint of transition and its slope, respectively. The midpoint of transition was determined and used with the Nernst equation and a standard electrode potential of CSH of −260 mV (39) to estimate the midpoint electrode potential of *At*KAT2. It was found to be −372 mV at pH 8.5 and −283 mV at pH 7.0. The electrode potential of *At*KAT2 was assumed to follow the −59 mV/pH unit correlation identified previously for thioredoxins (40, 41). Far UV CD spectra of 5 μM *At*KAT2 incubated with 10 mM CSH or 5 mM CSSC were recorded in the same buffer as described above at 25 °C in a Jasco J-810 CD spectrometer with a 1-mm light path quartz cuvette at 20 nm/min and 0.1-nm pitch, averaging 6 scans.

Crystallization—*Ha*KAT at 10 mg/ml in 20 mM Tris-HCl, 150 mM NaCl, 2 mM EDTA, 5% (v/v) glycerol, and 2 mM DTT, pH 9.0, was mixed in a 1:1 ratio with 20% (w/v) polyethylene glycol 3350, 0.2 M $Li(CH_3COO)_2$, and 0.002% (v/v) ethylene glycol and crystallized by vapor diffusion (hanging drop) against a reservoir containing 20% (w/v) polyethylene glycol 3350, 0.2 M $Li(CH_3COO)_2$, and 0.01 M taurine. The crystals were flash-frozen in liquid nitrogen using 30% (v/v) ethylene glycol as a cryoprotectant. *At*KAT2 at 11.8 mg/ml in 20 mM Tris-HCl, 150 mM NaCl, 2 mM EDTA, 5% (v/v) glycerol, and 2 mM DTT, pH 9.0, was mixed in a 1:1 ratio with 20% (w/v) polyethylene glycol 3350, 0.2 M $Li(CH_3COO)_2$, 0.002% (v/v) ethylene glycol, and 2 mM C12-CoA and crystallized by vapor diffusion (hanging drop) against a reservoir containing 20% (w/v) polyethylene glycol 3350 and 0.2 M $Li(CH_3COO)_2$. The crystals were flash-frozen in liquid nitrogen using 30% (v/v) ethylene glycol as cryoprotectant. In both cases crystals grew within 1 week.

X-ray Data Collection, Structure Solution, and Refinement—X-ray data collection and refinement details are given in Table 1; 5% of the reflections flagged for R_{free} were chosen in resolution shells using SFTOOL because of assumed non-crystallographic symmetry (NCS). A preliminary *Ha*KAT data set was collected in-house to 2.5 Å resolution (data not shown), and the *At*KAT2 (21) monomer was used as a search model for two molecules/asymmetric unit using PHASER (42). One clear solution resulted; this structure was used for refinement against the higher resolution *Ha*KAT (data reported here; the same R_{free} set was applied and extended). Initial rigid body refinement was performed treating each monomer as a rigid body. Cycles of restrained refinement including motions for translation/libration/screw (TLS) (four segments/chain, defined using the TLS server (43) and selected on B-factor distribution, resulting in one group for the N-terminal domain, two groups for the L-domain, and one group for the C-terminal domain) in Refmac (44, 45), the use of TLS lowered the R_{free} and R_{work} values. Medium NCS restraints (chains A and B) were used in

the initial rounds of refinement; these were loosened for the rest of the refinement. The main deviations between the molecules occurred in the positioning of the β-hairpin in the L-domain. Water molecule assignment and manual rebuilding was performed in COOT (46) It was noticed that the B-factors assigned to the water molecules during this TLS refinement were largely unexpected, which was also reflected in the electron density, with B-factors either suspiciously high with positive density or suspiciously low with negative density. This is reported as a possible "bug" in the current version of Refmac (version 5.5.0035). Therefore, the final rounds of refinement were performed in PHENIX (47) using the default settings, which resulted in more realistic B-factors and density for the water molecules. The *Ha*KAT dimer model was used as the search model for the *At*KAT2 data using PHASER and resulted in one clear solution. Refinement proceeded as per the *Ha*KAT structure. PDB coordinates and structure factors have been deposited with accession codes 2WUA and 2WU9 (deposited via the Protein Data Bank in Europe (PDBe)).

Co-Immunoprecipitation Studies—Enriched peroxisomal lysate was isolated in the following manner. Seedlings (*Brassica napus* cv.) were grown in the dark for 7 days; the cotyledons were then harvested, homogenized in 10 ml of 0.25 M sucrose, 0.1 M Tris-HCl, pH 7.4, 1 mM EDTA, 1 mM $MgCl_2$, 0.1% ethanol, and complete EDTA-free protease inhibitor (Roche Applied Science), and filtered through two layers of Myra cloth. Cell debris was removed by centrifugation at 600 × *g* for 5 min. Peroxisomes were sedimented by centrifugation (15,000 × *g*, 20 min), resuspended in 1 ml of 0.1 M Tris-HCl, pH 7.4, 1 mM EDTA, 1 mM $MgCl_2$, 150 mM NaCl, and complete EDTA-free protease inhibitor (Roche Applied Science), and incubated on ice for 20 min to lyse the peroxisomal membranes. The lysate was cleared twice by centrifugation at 15,000 × *g* for 20 min. The cleared lysate was then used for co-immunoprecipitation studies using the Seize X protein A kit (Pierce) following the manufacturer's guidelines, immobilizing antibodies against either KAT or MFP on the beads. The eluted antigens were run in duplicate on SDS-PAGE (4–12% bis-Tris, Invitrogen) and blotted onto nitrocellulose membranes. Western blots were then developed using polyclonal antibodies against either MFP or KAT as primary antibodies. The MFP antibodies were raised against recombinant *At*MFP2, and the KAT antibodies were raised against recombinant *B. napus* KAT2 (48). The *At*MFP2 antibodies have also been shown to cross-react with recombinant *At*AIM1. A control pulldown was performed using immobilized antibodies against His tags with the peroxisomal lysate.

Structure Analysis and Modeling—Secondary structure assignment and protein-protein interactions were defined using PROMOTIF (49) via the PDBsum server (50). To construct the *Arabidopsis* β-oxidation complex model based on the bacterial multi-enzyme β-oxidation complex, we simply superimposed the *At*MFP2 structure (51) onto the *Pf*MFP (chains A and B) and the *At*KAT2 dimer onto the *Pf*KAT (chains C and D; PDB code 1WDK) and then performed a simulated annealing energy minimization using the crystallography and NMR system (CNS) (52) to minimize clashes between side chains of the two proteins; backbone atoms remained unchanged. To look at the amino acid conservation of the prokaryotic *Pf*KAT and peroxisomal eukaryotic *At*KAT2, their sequences were subjected to a BLAST (53) search, and then unique sequences (56 for *Pf*KAT (sequence identity 57–99%) and 52 for *At*KAT2 (sequence identity 43–96%)) were compiled and aligned in ClustalW (54). These multiple sequence alignments were then used with their respective structures in ConSurf (55), the output of which allows coloring of the PDB files with respect to conservation, from blue (conserved) through the rainbow to red (unconserved). *Pf*KAT and *At*KAT2 structures were not used alone for ConSurf, as many unrelated thiolases were selected by the server. Instead, we opted to select a range of prokaryotic KATs for the *Pf*KAT and peroxisomal eukaryotic KATs for the *At*KAT2 to keep the comparison focused on the β-oxidation pathway. The *Pf*MFP and *At*MFP structures were subjected to the basic ConSurf 50-sequence selection with a PSI-BLAST E-value cut-off of 0.001. Analysis of the protein-protein interactions was aided by the use of PDBsum and PROTORP (56). Gap volume index values were calculated with PROTORP and NOXclass (57), where these values varied slightly (an average has been reported). Figs. 1, 4, and 5 were prepared using PyMOL. For clarity, for the online supplemental movie, a missing loop containing Trp^{175} in the $At\text{KAT2}_{\text{inactive}}$ structure has been modeled using Modeler 7v7 (58).

RESULTS

Crystal Structures of AtKAT2 and HaKAT—The crystal structures of *Arabidopsis* and *Helianthus* 3-ketoacyl-CoA thiolase have been solved in their dimeric, open, reduced, active state to high resolution (1.5 and 1.8 Å, respectively). *At*KAT2 consists of residues 46–448 (A) and 47–448 (B), and *Ha*KAT consists of residues 47–438 (A) and 45–438 (B). Data collection, refinement, and validation details are given in Table 1. To facilitate an easy reference system for the secondary structure elements, the sequences of *At*KAT2 and *Ha*KAT were aligned with sequences of other known KAT2 structures, namely from *A. thaliana* in the inactive form ($At\text{KAT2}_{\text{inactive}}$; PDB code 2C7Y (21)), *Homo sapiens (Hs*KAT; 2IIK), *S. cerevisiae* (*Sc*KAT; 1AFW (19)), and *P. fragi (Pf*KAT; 1WDK, chains C and D (16)). β-Strands and helices (α and 3_{10}) were defined using PDBsum (50), incorporated, and numbered according to domains (supplemental Fig. S1 online). The *At*KAT2 and *Ha*KAT structures reported here are very similar and exhibit the expected thiolase-like fold described for the *Sc*KAT structure (19). Each subunit consists of three domains (Fig. 1*A*); the N-domain and C-domain are related by a pseudo 2-fold axis and have the same α/β tertiary fold consisting of a central five-stranded β-sheet where the fifth strand is anti-parallel to strands 1–4. Two α-helices cover the outer side of the β-sheets, and one α-helix from each domain is buried between the sheets. The loop domain (L-domain) is composed of four α-helices (H2, H3, H4, and H5), two 3_{10}-helices (H1 and H6a), and a β-hairpin (S1 and S2; β-hairpin 1) that extends away from the globular protein by ~25 Å. The dimer (consisting of subunits A and B) is formed by interactions involving mainly the N-domains.

Subunit A superimposes onto subunit B with an r.m.s.d. of 0.3 Å over 403 Cα atoms in the *At*KAT2 structure and with an r.m.s.d. of 0.4 Å over 391 Cα atoms in the *Ha*KAT structure. As

TABLE 1
X-ray data collection, processing, and refinement statistics

Statistics	Data set	
	*Ha*KAT	*At*KAT2
Data collection and processing		
Collection site	ID23, ESRF, France	X12, DESY, Germany
Wavelength (Å)	0.9762	1.0
Space group	$P2_12_12_1$	$P2_1$
Unit cell dimensions	a = 78.6 Å; b = 100.7 Å; c = 105.3 Å	a = 60.8 Å; b = 86.7 Å; c = 72.7 Å; β = 106.7°
Resolution (Å)	78.6-1.8 (1.9-1.8)[a]	34.6-1.5 (1.58-1.5)[a]
R_{merge} (%)	8.6 (51.9)[a]	7.8 (50.0)[a]
R_{pim}[b]%	3.8 (26.9)[a]	3.1 (23.7)[a]
Mean (I)/S.D. mean (I)	18.0 (2.6)[a]	15.2 (2.6)[a]
Completeness (%)	99.2 (94.8)[a]	97.2 (81.2)[a]
No. of unique reflections	77,995	112,318
Multiplicity	8.2 (5.4)[a]	5.1 (4.3)[a]
Wilson B factor[c] (Å^2)	28.44	12.00
Refinement		
No. of non-hydrogen protein atoms	5,875	6,151
No. of water molecules	709	1,134
No. of ethylene glycol molecules	0	9
R_{work}[d] (%)	18.5 (24.4)[e]	14.9 (20.9)[e]
R_{free}[d] (%)	21.6 (28.6)[e]	17.7 (21.9)[e]
S.D.[d]		
Bond angles (°)	1.020	1.088
Bond lengths (Å)	0.006	0.006
Mean B[d] (Å^2)	33.4	14.3
Main chain (Å^2)	29.8	9.9
Side chains (Å^2)	34.3	14.0
Solvent (Å^2)	44.6	27.5
Ramachandran plot[f]		
Most favored (%)	91.8	93.4
Additionally allowed (%)	7.4	6.0
Generously allowed (%)	0.5[g]	0.3[g]
Disallowed (%)	0.3[h]	0.3[h]

[a] Numbers in parentheses refer to outer resolution bin.
[b] Multiplicity-weighted R_{merge} (66).
[c] From Truncate analysis (67).
[d] From phenix.refine (47).
[e] Highest resolution bin.
[f] From ProCheck (68).
[g] *Ha*KAT Gln^{135} and *At*KAT2 Gln^{137} adopt strained conformation in active site.
[h] *Ha*KAT Lys^{64} and *At*KAT2 Lys^{66} adopt strained conformation in well defined density in tight turn.

expected there are deviations in the position and quality of electron density at the very extremities of the N and C termini. There is some deviation in the orientation of β-hairpin 1, by as much as 5 Å in *At*KAT2, and small differences (~1 Å) in the α-helical region of the L-domain. Electron density is of a continuous high quality with only a few exceptions; the loop from the N-domain to the L-domain and the extremities of β-hairpin 1 are of poorer quality, and here side chains are defined only marginally. A mutation was also noticed in the *Ha*KAT electron density at position 223; this was confirmed by sequencing to be a threonine instead of an alanine. This residue is situated on H4 in the L-domain, and the mutation is not thought to have affected the overall structure because the *At*KAT2 and *Ha*KAT structures are almost identical as expected from their 85% sequence identity (dimer superimposes with an r.m.s.d. of 0.57 Å over 780 Cα atoms). *At*KAT2 and *Ha*KAT exhibit only small differences in two loops; a movement of the β-hairpin 1 in subunit B that results in a Cα difference in position of ~7 Å at the tip of the loop ($Lys^{247}{}_{AtKAT2}$ *versus* $Lys^{249}{}_{HaKAT}$). This difference is only ~1 Å in the A subunits, suggesting a crystal packing influence. To a much lesser extent there is also a variation in the loop between the N-domain and the L-domain. There is an additional α-helix (H6a) in the C-domain of *At*KAT2 that is not observed in *Ha*KAT or in any of the other type I thiolase structures. In addition to the side chains, which are different between these two proteins, a few changes in main chain positions and side chain orientations can be observed, mainly in solvent-exposed areas of the structures. Fig. 1*B* shows a superposition of all type I thiolase structures available; these are compared in more detail in supplemental Table S1 and Fig. S1.

AtKAT2 Redox Potential and Activity—Sundaramoorthy *et al.* (21) suggest that the oxidized form found in their *At*KAT2 crystals represents an inactive state of a biologically relevant redox switch regulating peroxisomal β-oxidation in *Arabidopsis*; however, no data are presented bridging the form found in their crystal structure to activity. Our activity data (Fig. 2*A*) show that *At*KAT2 was inactivated, with a half-life of 0.6 h, in the presence of the oxidant CSSC (10 mM), whereas in the presence of the reductant CSH (20 mM) full activity was retained for more than 12 h (data not shown). In the absence of both CSSC and CSH, *At*KAT2 was spontaneously inactivated with a half-life of 2.6 h, indicating a very low reduction potential. To investigate this further, tryptophan fluorescence was recorded while titrating the enzyme with CSH. Trp^{175} is the only tryptophan residue in *At*KAT2. Buried at the surface near the active site and the subunit interface, it is optimally positioned to report fluorescently on the redox-coupled rearrangement of the molecule (supplemental movie online). The tryptophan fluorescence of *At*KAT2 increases with increasing $[CSH]^2/[CSSC]$ ratios (Fig. 2*B*). The increase is accompanied by a small red shift of the

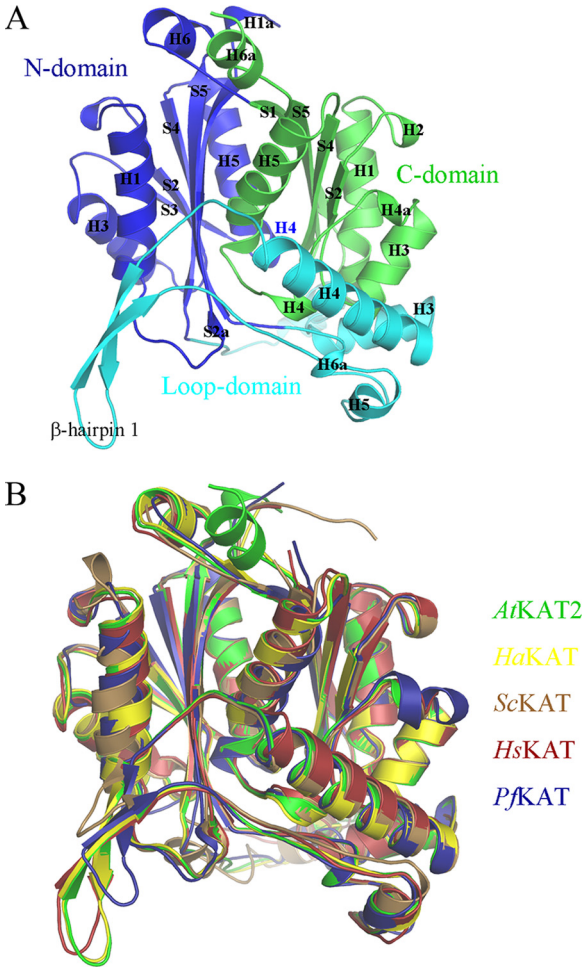

FIGURE 1. **The structure of KAT.** *A*, schematic of *At*KAT2 monomer: N-domain is shown in *dark blue*, C-domain in *green*, and L-domain in *cyan*. The secondary structure elements are labeled. *B*, superposition of KATs in open conformation. The r.m.s.d. values and sequence identities are given in supplemental Table S1. A detailed comparison of these structures is also included in the supplemental material (Discussion Fig. S1, and Table S1).

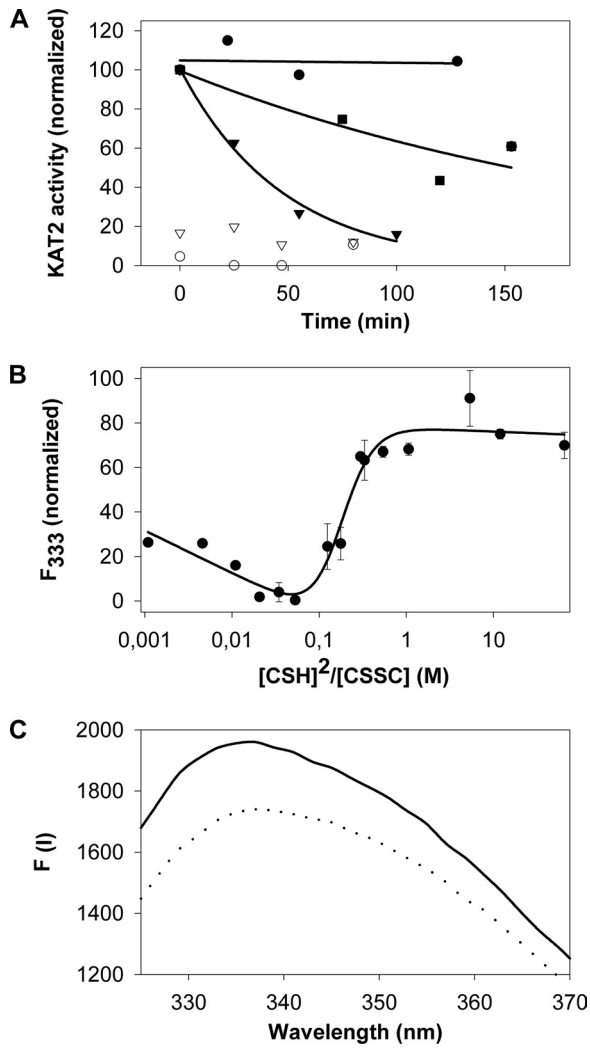

FIGURE 2. **Characterization of redox state dependent activity.** *A*, *At*KAT2 is inactive in the presence of CSSC and active in the presence of CSH. The rates of acetoacetyl-CoA cleaving by *At*KAT2 were determined as a function of time and incubation with oxidant or reductant. 12.5 μM enzyme preparations were incubated at 25 °C in 35 mM Tris (pH 8.5), 0.1 M NaCl and 20 mM CSH (●), 10 mM CSSC (▼) or buffer (■). The effects of CSH (○) and CSSC (▽) on the substrate are included for reference. The incubations were sampled at the given time points by rapid mixing and 2500× dilution with 100 μM CoA, 50 μM acetoacetyl-CoA in a microcuvette with absorbance recorded at 233 nm. The final concentrations of *At*KAT2, CSH, and CSSC in the reactions were 5, 8, and 4 nM, respectively. *B*, *At*KAT2 changes tertiary structure upon incubation with CSSC. *At*KAT2 was incubated with different ratios of $[CSH]^2/[CSSC]$ at 25 °C for 10 min, and tryptophan fluorescence was recorded at 333 nm with excitation wavelength 285 nm. The total concentration of CSH and CSSC was kept constant at 125 mg/liter. A two-state equation was fitted to the normalized (solid line) data and the midpoint of transition determined. *C*, Fluorescence spectra of reduced (*solid line*) and oxidized (*dotted line*) *At*KAT2 at 1 and 0.03 M $[CSH]^2/[CSSC]$, respectively. Conditions as in *B* except emission recorded from 325 to 450 nm.

emission (Fig. 2*C*) in accord with a slightly higher degree of solvation of Trp^{175} in the open, active conformation. Adding β-mercaptoethanol to the solution resulted in a similar increase, whereas adding H_2O_2 resulted in a decrease. Comparing the overall secondary structure content of $AtKAT2_{active}$ and the oxidized $AtKAT2_{inactive}$, there is a mere 2.4% difference in the α-helical content in favor of the $AtKAT2_{active}$ and 2.5% more β-structure in the $AtKAT2_{inactive}$. The CD spectra of oxidized and reduced *At*KAT2 differed insignificantly, supporting the interpretation that the fluorescence signals represent the local rearrangements observed in the $AtKAT2_{inactive}$ and $AtKAT2_{active}$ crystal structures (see supplemental movie and "Discussion" online). The transition midpoint between the two states is 0.17 ± 0.02 M, which by using the Nernst equation gives an E_m at pH 8.5 of −372 mV equal to E_0 of −283 mV at pH 7.0 (assuming linear proportionality with pH with a slope of −59 mV in this pH range (40, 41)), indicating that this redox potential falls within a physiological range (see "Discussion" below).

Potential of KAT to Form a Multi-enzyme Complex with MFP—The existence of multifunctional enzymes harboring the last three enzymatic steps of β-oxidation in bacteria and mitochondria led us to investigate whether a similar trifunctional complex exists in plants. We employed pulldown assays from enriched peroxisomal lysate isolated from *B. napus* cv. seedlings and focused on a possible interaction between MFP2 and KAT2. *Brassica* and *Arabidopsis* both belong to the monophyletic family of the Brassicaceae and share a recent common ancestry ending about 20 million years ago (59). The *Bn*KAT2 and *At*KAT2 sequences are 96% identical and the *Bn*MFP2 and

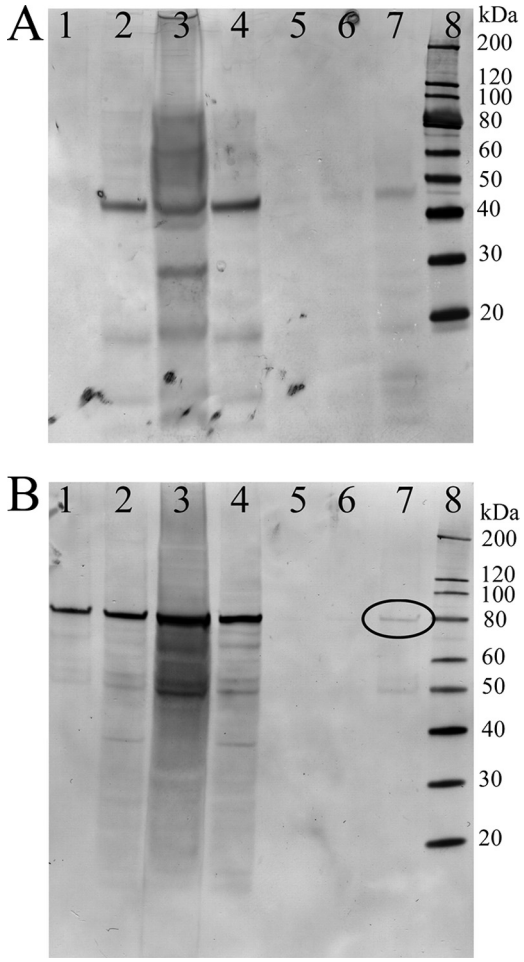

FIGURE 3. **Western blot analysis from co-immunoprecipitation studies.** *Lanes* contained the following: *lane 1*, elution 1 from MFP beads; *lane 2*, load onto MFP beads; *lane 3*, peroxisomal lysate; *lane 4*, load onto KAT beads; *lane 5*, elution 3 from KAT beads; *lane 6*, elution 2 from KAT beads; *lane 7*, elution 1 from KAT beads; *lane 8*, molecular weight marker. *A*, Western blot developed with primary antibody against KAT. *B*, Western blot developed with primary antibody against MFP. A band is seen for MFP from the KAT2 pulldown suggesting a complex (*black circle*). Elution steps were performed only after extensive washing.

*At*MFP2 sequences are 90% identical. When *Bn*KAT2 antibodies were immobilized for co-immunoprecipitation, both *Bn*KAT2 and *At*MFP2 antibodies identified bands of an appropriate molecular weight on the resulting Western blot (see Fig. 3), suggesting that these proteins interact. However, when *At*MFP2 antibodies were immobilized, only the *At*MFP2 antibodies identified a band on the Western blot, suggesting that KAT2 was not pulled down with MFP2. The inability of the anti-*At*MFP2 to co-immunoprecipitate *Bn*KAT2 does not discredit the existence of the complex, as the antibodies may disrupt the interaction. When a negative control using an unrelated antibody, anti-His, in place of the antibodies against KAT2 and MFP2 for the pulldown was performed and Western blots were developed using antibodies against KAT2 and MFP2, no bands were identified (data not shown).

DISCUSSION

Redox Regulation of AtKAT2 and Comparison of Active and Inactive Structures—The redox potential of the peroxisomes has not been determined quantitatively, but the redox potential in living plant cells has been determined to be about −320 mV in the cytosol at pH 7.2 and −360 mV in the mitochondria at pH 8.0 (60). Assuming that the peroxisomes can attain a redox potential similar to that of the mitochondria, the ratio between oxidized and reduced *At*KAT2 at thermodynamic equilibrium would be 0.24 at pH 8.5, whereas at −340 mV it would be 99% oxidized. Other dithiols have been suggested to be redox sensors; the disulfides of Orp1 and the redox-sensing domain of the cytosolic Yap1 have potentials as low as −315 and −330 mV at pH 7.0 (61), whereas the potential of the active cysteines of wild-type plant cytosolic thioredoxins varies from −280 to −304 mV at pH 7.0 (62). Yap1 is thought to be kept in the reduced state by the non-equilibrium ratios of 10^2 to 10^4 reduced:oxidized thioredoxin existing in the cells. Although a recent proteomics study identified two putative thioredoxins and a glutathione reductase in *Arabidopsis* peroxisomes (63), there is little knowledge about disulfide reducing agents in the peroxisomes. Overall, it is likely that *At*KAT2 represents a very sensitive redox switch capable of regulating β-oxidation even at minor perturbations of the peroxisomal redox environment. Interestingly, it has been observed that the activity of KAT is compromised by 0.1 mM H_2O_2 in catalase-inhibited enzyme preparations from peroxisomes of rat liver (64). It therefore seems likely that the oxidized and reduced forms of *At*KAT2, crystallized under different conditions, represent biologically relevant forms of *At*KAT2.

When comparing the *At*KAT2$_{active}$ (this study) and *At*KAT2$_{inactive}$ (PDB code 2C7Y (21)) structures, there are a number of differences. At the monomer level Asp^{38}–Asp^{51} in the *At*KAT2$_{inactive}$ structure form a β-strand (S1a), which affiliates with the C-terminal domain and pairs up with the equivalent strand in the dimer formation (supplemental movie online), resulting in an extended central β-sheet. β-Strand S1a is not seen in the *At*KAT2 structure described here, and despite the residues being present in the construct, they are unseen in the electron density. One reason for this difference could be the presence of the N-terminal His$_6$ tag in our construct; however, we think this is an unlikely explanation, as the equivalent residues are present in the *Ha*KAT construct and are also unseen in the structure where there is no N-terminal His$_6$ tag. The β-strand formation is therefore more likely the result of the dimer reorientation in the oxidized form of *At*KAT2, caused by the disulfide bridge formation. The inactive conformation provides a different interface that allows stabilization of the otherwise flexible chain, providing more interaction. The active site loop in the inactive form, between β-strand S3 and α-helix H5 in the N-domain, is flipped out toward subunit B, repositioning the Cys^{138} Cα by 5.4 Å (superimposing A chains) or 5.8 Å (superimposing B chains) away from the helix dipole, which is important for the activation of Cys^{138} (20). The short 3_{10}-helix (N-domain H4) containing the active site cysteine, present in all of the active structures, is not observed in the *At*KAT2$_{inactive}$ structure. The location of this loop segment in *At*KAT2$_{inactive}$ would cause steric clashes with β-strand S3 in the N-domain and the preceding loop on subunit B in the active dimer. As such, subunit B is repositioned in the *At*KAT2$_{inactive}$ dimer via a rotation of ~30° and translation of ~10 Å (supplemental movie online). The Met^{168}–Pro^{195} region in *At*KAT2$_{active}$ L-domain

caps over the S2a-H1 loop and α-helix H3 in subunit B N-domain and contains a short 3_{10}-helix (H1) and an α-helix (H2). In the *At*KAT2$_{inactive}$ structure, this loop is largely disordered, with Met^{173}–Lys^{184} not seen in the structure and residues Met^{168}–Pro^{172} extending out toward where α-helix H1 in the L-domain is positioned in *At*KAT2$_{active}$. In *At*KAT2$_{inactive}$, H2 and H3 in the L-domain form one continuous α-helix via a flip of Pro^{195}, which is then, remarkably, incorporated into the α-helix reorienting the polypeptide such that Cys^{192} is repositioned by ~9.5 Å (supplemental movie online). The large conformational change of this region (C terminus of N-domain S4 to N terminus of C-domain H4), upon the disulfide bridge formation, results in the domain reorientation. β-Hairpin 1 in the L-domain and S1-H1a in the C-domain have a difference in position of ~6 Å, and β-hairpin 2 has a difference of ~3 Å. When superimposing the B subunits there is an alternative movement in β-hairpin 1; Lys^{249} Cα is positioned 2.8 Å in the opposite direction to the 7 Å movement observed in this loop in the *Ha*KAT structure suggesting that this is highly mobile. The 3_{10}-helix, H6a (observed in *At*KAT2$_{active}$, *Ha*KAT, and *Pf*KAT), in the L-domain is not observed in the inactive form; it is replaced with two β-turns, as in the *Hs*KAT and *Sc*KAT structures.

The *At*KAT2$_{inactive}$ dimer is very different from all other KAT structures and has roughly half the amount of intersubunit contacts as the active dimers. Twenty-six residues from each chain are involved, giving an interacting surface area of 1225 Å^2 with 11 hydrogen bonds and 168 non-bonded contacts compared with 54 residues from each chain with an interacting surface area of 2500 Å^2, 41 hydrogen bonds, and 408 non-bonded contacts (values calculated in PDBsum) for the *At*KAT2$_{active}$ dimer. In addition, the gap volume index (this gives an indication of how well the two protomers fit together, with a lower number indicating a better fit) is 3.9 Å for the inactive form and 2.3 Å for the active form; and the interprotomer salt bridges that are present in all of the active KAT structures (Asp^{99}–Arg^{136} and Arg^{132}–Asp^{147} (*At*KAT2 numbering)) are not formed in the *At*KAT2$_{inactive}$ conformation. This strongly suggests that the active, reduced conformation is the most stable dimer form. If we look at the isoforms present in *Arabidopsis*, both *At*KAT1 and *At*KAT5 possess the Cys^{192} and Pro^{195} and so are also likely to be regulated via their redox environment. In contrast, *At*ACAT1 and *At*ACAT2 (responsible for the reverse reaction and sharing 34 and 36% sequence identity with *At*KAT2) do not have these residues, suggesting that the reverse reaction (Claisen condensation) is not regulated by redox. Cys^{192} and Pro^{195} are conserved in all non-mitochondrial eukaryotic KATs in which they have been sought. However, these residues are absent in the prokaryotic and mitochondrial KATs, thus revealing a very distinct, perhaps evolutionary, difference (peroxisome *versus* mitochondrion) in the regulation of β-oxidation.

Model of Plant β-Oxidation Multi-enzyme Complex—The crystal structures of the plant KATs presented here and the crystal structure of *At*MFP2 (presented in an accompanying paper (Arent *et al.* (51)) bear close resemblance in structure to the components of the bacterial β-oxidation multi-enzyme complex from *Pseudomonas* (PDB codes 1WDK, 1WDL, 1WDM, and 2D3T (16)). The *Pseudomonas* complex is composed of two MFP subunits (1WDK superimposes with *At*MFP with an r.m.s.d. of 1.9 Å over 1406 residues; sequence identity 31%) and two KAT subunits (Fig. 4*A*) constituting a dimer that is indistinguishable from that of the reduced plant *At*KAT2$_{active}$ structure (1WDK superimposes with an r.m.s.d. of 1.2 Å over 735 amino acids; sequence identity 42%). The interactions between the two MFPs and between the MFP and KAT subunits in the *Pseudomonas* structure are quite small in surface area but collectively form a stable complex that can withstand purification via gel filtration (16, 65). In addition, substrate-dependent conformational changes are seen within the *Pseudomonas* tri-complex, mainly involving the MFPs (compare PDB 1WDK with 2D3T for extremities), but the protein-protein interactions remain constant. Our co-immunoprecipitation experiments suggest an interaction between MFP and KAT in plants, and thus we were encouraged to see whether a complex similar to the *Pseudomonas* multi-enzyme complex could be

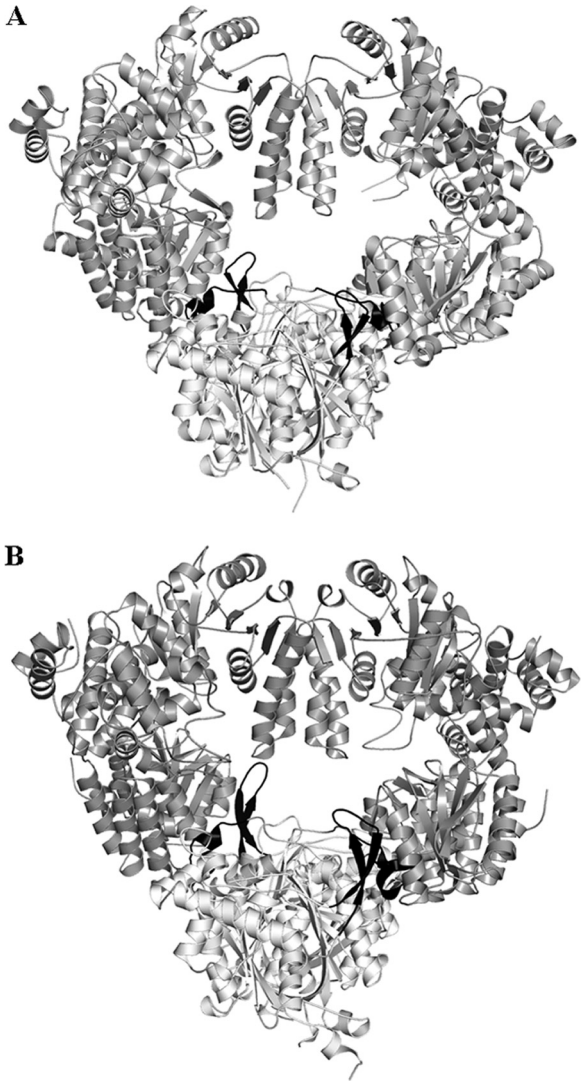

FIGURE 4. **Construction of the *Arabidopsis* KAT2·MFP2 complex model based on the prokaryotic multi-enzyme complex (PDB code 1WDK).** *A*, *Pseudomonas* structure with MFP in *medium gray* and KAT in *light gray*. Region 1 (α-helical) and region 2 (β-hairpin 1) are highlighted in *black*. *B*, *Arabidopsis* model follows the same coloring scheme as *A* with *At*MFP2 in *medium gray* and *At*KAT2 dimer in *light gray*.

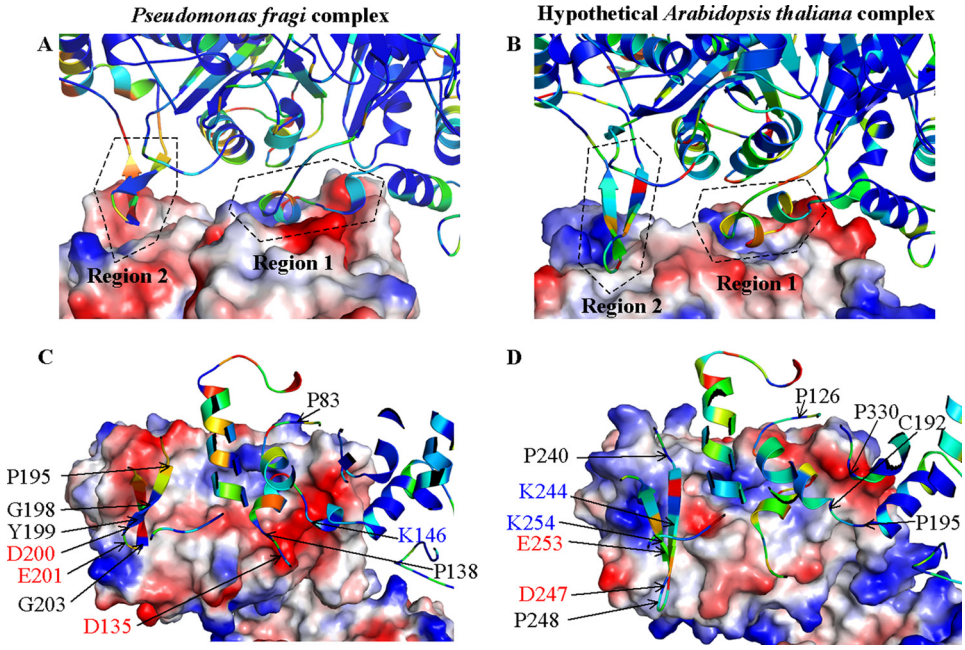

FIGURE 5. **Comparison of prokaryotic multi-enzyme complex with model complex of *At*KAT2 and *At*MFP2.** *A* and *C*, *Pseudomonas* structure. *B* and *D*, *Arabidopsis* model. *Pf*MFP and *At*MFP are shown as an electrostatic surface colored according to electrostatic potential (from *red* (most electronegative) to *white* to *blue* (most electropositive)). *Pf*KAT and *At*KAT2 are shown as a rainbow-colored schematic according to conservation among prokaryotic and plant KATs, respectively (from *blue* (most conserved) to *green* to *yellow* to *red* (unconserved)).

modeled from our *Arabidopsis* KAT2 and MFP2 crystal structures (see "Experimental Procedures" for details and Fig. 4). A complex between MFP2 and KAT2 would allow metabolite channeling, facilitating the product of one enzyme action to be transferred directly to the next in the cycle without either the equilibration of the intermediate with the bulk solvent or the pursual of an alternative pathway. Additionally, the lack of substrate specificity at the final thiolytic step of the pathway is consistent with the idea of substrate channeling while allowing the redox control of the cycle as a whole in response to H_2O_2 levels.

In the *Pseudomonas* structures, both MFP subunits interact with both KAT subunits, although the interacting surface areas are small (500–850 Å^2). There are two regions in the L-domain of the KAT subunits that interact with MFP subunits (Fig. 5): Region 1 is composed of H1-H2 and has an interaction surface area of ~800 Å^2 and a gap volume index of 2.5 Å, indicating a favorable complementary shape. Region 2 involves β-hairpin 1 from the KAT subunit and has an interaction surface area of ~550 Å^2 and a gap volume index of 7 Å, indicating a loose, less complementary shaped interaction than that of Region 1. There are few hydrogen bonds, some favorable electrostatic interactions, but no salt bridges at this interface. The size and limited specific interactions suggest that this complex could be fairly transient *in vivo*. In region 1, H2 and the C terminus of S1 are well conserved in the prokaryotic KATs; however, H1 and the rest of the β-hairpin 1 seem to be fairly variable (Fig. 5). Electrostatic interactions are evident between Lys^{146} of H2 and the conserved negative surface of the *Pf*MFP (Asp^{162} and Glu^{166}) (Fig. 5, *A* and *C*). Asp^{200} in the β-hairpin is in the vicinity of a positively charged patch on the surface of the MFP in the case of *Pseudomonas*. However, this positive area is not at all conserved, and in the structures available no hydrogen bond interactions were observed. Asp^{135}, in the loop preceding H1, is actually situated near a negatively charged area of the MFP. Overall, the interactions between region 1 in the KAT with the MFP are more substantial when compared with region 2 with respect to surface area, conservation, and complementary shape.

In comparison, the complex modeled for *At*KAT2 and *At*MFP2 is fairly similar. The calculated interaction surface area overall in the *Arabidopsis* model is actually larger than in the *Pseudomonas* structure, with region 1, the H1-H2 region, involved in an interface of ~750 Å^2 and region 2, the β-hairpin, involved in an interface of ~920 Å^2. However, the shape fit of region 1 is not as favorable as that in the *Pseudomonas* structure, with a gap volume index of 4 Å. Region 2, which is more extensive in the *Arabidopsis* model, has a gap volume of 4.3 Å, which is more sustainable as a contact than this region in the *Pseudomonas* structure (7 Å); residues are similarly conserved. It should be noted that upon actual complex formation, small movements may occur providing a different fit than our simple model. β-Hairpin 1 is longer in *At*KAT2 and thus has the potential to make a larger interface with *At*MFP2. Lys^{244} on S1 is positioned nicely to form an electrostatic interaction with the indented negative surface of MFP2 (Asp^{185}; Fig. 5*D*), and these residues are conserved in plant KAT/MFPs. In the case of *Arabidopsis*, there is even a potential for a salt bridge formation between Glu^{253} on S2 and His^{179} in *At*MFP2. Although these residues are not 100% conserved among plant MFP/KATs, the charges are more so with the glutamic acid well conserved and histidine sometimes replaced by arginine.

There are a number of conserved proline residues in the vicinity of the interface that could be key to adding structural rigidity to the loops involved in the interaction with MFP2 (Fig. 5, *C* and *D*). The potential electrostatic interaction for Lys^{146} seen in the *Pseudomonas* structure does not exist in the case of the *Arabidopsis* model, as there is no charged residue at that position and also the surface potential of *At*MFP2 is not negative in that area. Indeed, the *At*MFP2 area around H2 is largely neutral in surface potential compared with the negative patch seen in *Pseudomonas*. Overall, the *Arabidopsis* model exhibits more electrostatic potential (10–20% more charged residues at interface) at each of the interfaces than the *Pseudomonas* structure, which could play a role in interaction specificity of the isoforms in *Arabidopsis* and may make the complex less tightly bound in conventional protein extraction procedures. In addition, in plants there is the potential to form cation-pi interac-

tions between a highly conserved Lys^{281} in *At*KAT2 with Phe^{233} in *At*MFP2 (conserved in plant MFP2-like but not AIM1-like isoforms). Thus, we propose that a similar interaction to that found in *Pseudomonas* could exist between KAT2 and MFP2 in the peroxisomal plant system; however, we would suggest that β-hairpin 1 (region 2) plays a more significant role in *Arabidopsis* than in the *Pseudomonas* complex.

Interestingly, it is the H2 in region 1 of the proposed *Arabidopsis* complex that hosts Cys^{192}, which is involved in the disulfide bridge formation with the active site cysteine in the redox regulation (see above). The redox control in the peroxisomal KATs could provide a reason why the interaction with MFP2 in this H1-H2 region is not as prominent as it is in the *Pseudomonas* structure, because when the dimer undergoes conformational change this area is affected most and consequently needs to be more malleable. When the KAT dimer is inactivated and is in the closed conformation, this would either force a rearrangement of the MFP·MFP interface or, more likely, break the MFP·KAT complex altogether. To make up for this region needing to be flexible, the extended β-hairpin in plant peroxisomal KATs would allow for an additional, compensating surface area for the interaction to achieve stability.

In conclusion, β-oxidation of fatty acids is a fundamental process that occurs in peroxisomes and plays essential roles at all stages of plant life from germination to the mature plant. We have demonstrated that the peroxisomal thiolytic cleavage of the two-carbon unit, the last step of the β-oxidation cycle, is controlled by a sensitive redox switch that could be physiologically relevant with regard to the environment of the peroxisome. The direct communication between the breakdown of fatty acids with other cellular activities such as neutralization of toxic substances, H_2O_2 signaling, and stress responses is of key importance for the viability of the cell and, indeed, the plant. The structures described here allow for a comparison with 3-ketoacyl-CoA thiolases from other species, a discussion on substrate binding, and a complete description of the large conformational change that occurs between the active and inactive forms of the thiolase. In addition, we have modeled a complex with the *At*MFP2 structure that would allow substrate channeling resulting in a highly efficient metabolon in a reducing environment that would however be destroyed in an oxidative environment.

Acknowledgments—We thank beamline scientists at stations X12, DESY, Hamburg, and ID23, ESRF, France for technical assistance during data collection. We thank Annette Kure Andreassen for general laboratory assistance, and we are also very grateful to Dr. Anders Brandt, Carlsberg Laboratory, for the BnKAT antibody.

REFERENCES

1. Knoop, F. (1905) *Beitr. Chem. Physiol. Pathol.* **6,** 150–162
2. Hooks, M. A., Bode, K., and Couée, I. (1996) *Biochem. J.* **320,** 607–614
3. van Roermund, C. W., Waterham, H. R., Ijlst, L., and Wanders, R. J. (2003) *Cell Mol. Life Sci.* **60,** 1838–1851
4. Kindl, H. (1987) in *The Biochemistry of Plants*, Stumpf, P.K., and Vol.9, pp. 31–52, Academic Press, London
5. Hayashi, M., Toriyama, K., Kondo, M., and Nishimura, M. (1998) *Plant Cell* **10,** 183–195
6. Germain, V., Rylott, E. L., Larson, T. R., Sherson, S. M., Bechtold, N., Carde, J. P., Bryce, J. H., Graham, I. A., and Smith, S. M. (2001) *Plant J.* **28,** 1–12
7. Delker, C., Zolman, B. K., Miersch, O., and Wasternack, C. (2007) *Phytochemistry* **68,** 1642–1650
8. Zolman, B. K., Martinez, N., Millius, A., Adham, A. R., and Bartel, B. (2008) *Genetics* **180,** 237–251
9. Neill, S., Desikan, R., and Hancock, J. (2002) *Curr. Opin. Plant Biol.* **5,** 388–395
10. Eccleston, V. S., and Ohlrogge, J. B. (1998) *Plant Cell* **10,** 613–622
11. Eastmond, P. J., and Graham, I. A. (2000) *Biochem. Soc. Trans.* **28,** 95–99
12. Richmond, T. A., and Bleecker, A. B. (1999) *Plant Cell* **11,** 1911–1924
13. Carrie, C., Murcha, M. W., Millar, A. H., Smith, S. M., and Whelan, J. (2007) *Plant Mol. Biol.* **63,** 97–108
14. Van Veldhoven, P. P., Vanhove, G., Assselberghs, S., Eyssen, H. J., and Mannaerts, G. P. (1992) *J. Biol. Chem.* **267,** 20065–20074
15. Ishikawa, M., Mikami, Y., Usukura, J., Iwasaki, H., Shinagawa, H., and Morikawa, K. (1997) *Biochem. J.* **328,** 815–820
16. Ishikawa, M., Tsuchiya, D., Oyama, T., Tsunaka, Y., and Morikawa, K. (2004) *EMBO J.* **23,** 2745–2754
17. Eaton, S., Bursby, T., Middleton, B., Pourfarzam, M., Mills, K., Johnson, A. W., and Bartlett, K. (2000) *Biochem. Soc. Trans.* **28,** 177–182
18. Yao, K. W., and Schulz, H. (1996) *J. Biol. Chem.* **271,** 17816–17820
19. Mathieu, M., Modis, Y., Zeelen, J. P., Engel, C. K., Abagyan, R. A., Ahlberg, A., Rasmussen, B., Lamzin, V. S., Kunau, W. H., and Wierenga, R. K. (1997) *J. Mol. Biol.* **273,** 714–728
20. Mathieu, M., Zeelen, J. P., Pauptit, R. A., Erdmann, R., Kunau, W. H., and Wierenga, R. K. (1994) *Structure* **2,** 797–808
21. Sundaramoorthy, R., Micossi, E., Alphey, M. S., Germain, V., Bryce, J. H., Smith, S. M., Leonard, G. A., and Hunter, W. N. (2006) *J. Mol. Biol.* **359,** 347–357
22. Schrader, M., and Fahimi, H. D. (2006) *Biochim. Biophys. Acta* **1763,** 1755–1766
23. Willekens, H., Chamnongpol, S., Davey, M., Schraudner, M., Langebartels, C., Van Montagu, M., Inzé, D., and Van Camp, W. (1997) *EMBO J.* **16,** 4806–4816
24. Mueller, S., Weber, A., Fritz, R., Mütze, S., Rost, D., Walczak, H., Völkl, A., and Stremmel, W. (2002) *Biochem. J.* **363,** 483–491
25. Fritz, R., Bol, J., Hebling, U., Angermüller, S., Völkl, A., Fahimi, H. D., and Mueller, S. (2007) *Free Radic. Biol. Med.* **42,** 1119–1129
26. Nyathi, Y., and Baker, A. (2006) *Biochim. Biophys. Acta* **1763,** 1478–1495
27. Cheeseman, J. M. (2006) *J. Exp. Bot.* **57,** 2435–2444
28. Simova-Stoilova, L., Demirevska, K., Petrova, T., Tsenov, N., and Feller., U. (2009) *Plant Growth Regul.* **58,** 107–117
29. Dansen, T. B., and Wirtz, K. W. (2001) *IUBMB Life* **51,** 223–230
30. Lardinois, O. M., and Rouxhet, P. G. (1996) *Biochim. Biophys. Acta* **1298,** 180–190
31. Kirkman, H. N., Galiano, S., and Gaetani, G. F. (1987) *J. Biol. Chem.* **262,** 660–666
32. Altomare, R. E., Greenfield, P. F., and Kittrell, J. R. (1974) *Biotechnol. Bioeng.* **16,** 1675–1680
33. Chance, B. (1952) *Arch. Biochem. Biophys.* **41,** 404–415
34. Nicholls, P., and Schonbaum, G. R. (1963) in *The Enzymes*, 2nd Ed., pp. 147–225, Academic Press, New York
35. Sinclair, A. M., Trobacher, C. P., Mathur, N., Greenwood, J. S., and Mathur, J. (2009) *Plant J.* **59,** 231–242
36. Schiedel, A. C., Oeljeklaus, S., Minihan, P., and Dyer, J. H. (2004) *Protein Expr. Purif.* **33,** 25–33
37. Lazarow, P. B. (1978) *J. Biol. Chem.* **253,** 1522–1528
38. Dawson, R. M., Elliott, D. C., Elliott, W. H., and Jones, K. M. (1974) *Data for Biochemical Research*, 2nd Ed., pp. 191–215, Oxford University Press, Oxford, United Kingdom
39. Millis, K. K., Weaver, K. H., and Rabenstein, D. L. (1993) *J. Org. Chem.* **58,** 4144–4146
40. Setterdahl, A. T., Chivers, P. T., Hirasawa, M., Lemaire, S. D., Keryer, E., Miginiac-Maslow, M., Kim, S. K., Mason, J., Jacquot, J. P., Longbine, C. C., de Lamotte-Guery, F., and Knaff, D. B. (2003) *Biochemistry* **42,** 14877–14884
41. Dutton, P. L. (1978) *Methods Enzymol.* **54,** 411–435

42. Read, R. J. (2001) *Acta Crystallogr. D Biol. Crystallogr.* **57,** 1373–1382
43. Painter, J., and Merritt, E. A. (2006) *Acta Crystallogr. D Biol. Crystallogr.* **62,** 439–450
44. Murshudov, G. N., Vagin, A. A., and Dodson, E. J. (1997) *Acta Crystallogr. D Biol. Crystallogr.* **53,** 240–255
45. Winn, M. D., Isupov, M. N., and Murshudov, G. N. (2001) *Acta Crystallogr. D Biol. Crystallogr.* **57,** 122–133
46. Emsley, P., and Cowtan, K. (2004) *Acta Crystallogr. D Biol. Crystallogr.* **60,** 2126–2132
47. Adams, P. D., Grosse-Kunstleve, R. W., Hung, L. W., Ioerger, T. R., McCoy, A. J., Moriarty, N. W., Read, R. J., Sacchettini, J. C., Sauter, N. K., and Terwilliger, T. C. (2002) *Acta Crystallogr. D Biol. Crystallogr.* **58,** 1948–1954
48. Olesen, C., Thomsen, K. K., Svendsen, I., and Brandt, A. (1997) *FEBS Lett.* **412,** 138–140
49. Hutchinson, E. G., and Thornton, J. M. (1996) *Protein Sci.* **5,** 212–220
50. Laskowski, R. A., Hutchinson, E. G., Michie, A. D., Wallace, A. C., Jones, M. L., and Thornton, J. M. (1997) *Trends Biochem. Sci.* **22,** 488–490
51. Arent, S., Christensen, C. E., Pye, V. E., Nørgaad, A., and Henriksen, A. (2010) *J. Biol. Chem.* **285,** 24066–24077
52. Brünger, A. T., Adams, P. D., Clore, G. M., DeLano, W. L., Gros, P., Grosse-Kunstleve, R. W., Jiang, J. S., Kuszewski, J., Nilges, M., Pannu, N. S., Read, R. J., Rice, L. M., Simonson, T., and Warren, G. L. (1998) *Acta Crystallogr. D Biol. Crystallogr.* **54,** 905–921
53. Altschul, S. F., Gish, W., Miller, W., Myers, E. W., and Lipman, D. J. (1990) *J. Mol. Biol.* **215,** 403–410
54. Thompson, J. D., Higgins, D. G., and Gibson, T. J. (1994) *Nucleic Acids Res.* **22,** 4673–4680
55. Landau, M., Mayrose, I., Rosenberg, Y., Glaser, F., Martz, E., Pupko, T., and Ben-Tal, N. (2005) *Nucleic Acids Res.* **33,** "Web Server Issue," W299–W302
56. Reynolds, C., Damerell, D., and Jones, S. (2009) *Bioinformatics* **25,** 413–414
57. Zhu, H., Domingues, F. S., Sommer, I., and Lengauer, T. (2006) *BMC Bioinformatics* **7,** 27
58. Sali, A., and Blundell, T. L. (1993) *J. Mol. Biol.* **234,** 779–815
59. Koch, M., Haubold, B., and Mitchell-Olds, T. (2001) *Am. J. Bot.* **88,** 534–544
60. Schwarzländer, M., Fricker, M. D., Müller, C., Marty, L., Brach, T., Novak, J., Sweetlove, L. J., Hell, R., and Meyer, A. J. (2008) *J. Microsc.* **231,** 299–316
61. Mason, J. T., Kim, S. K., Knaff, D. B., and Wood, M. J. (2006) *Biochemistry* **45,** 13409–13417
62. Bréhélin, C., Laloi, C., Setterdahl, A. T., Knaff, D. B., and Meyer, Y. (2004) *Photosynth. Res.* **79,** 295–304
63. Reumann, S., Quan, S., Aung, K., Yang, P., Manandhar-Shrestha, K., Holbrook, D., Linka, N., Switzenberg, R., Wilkerson, C. G., Weber, A. P., Olsen, L. J., and Hu, J. (2009) *Plant Physiol.* **150,** 125–143
64. Hashimoto, F., and Hayashi, H. (1987) *Biochim. Biophys. Acta* **921,** 142–150
65. Tsuchiya, D., Shimizu, N., Ishikawa, M., Suzuki, Y., and Morikawa, K. (2006) *Structure* **14,** 237–246
66. Evans, P. (2006) *Acta Crystallogr. D Biol. Crystallogr.* **62,** 72–82
67. French, S., and Wilson, K. (1978) *Acta Crystallogr. Sect. A* **34,** 517–525
68. Laskowski, R. A., Moss, D. S., and Thornton, J. M. (1993) *J. Mol. Biol.* **231,** 1049–1067